Measurement Report for the Four-Rod LHC Crab Cavity. Cold Tests held in July 2014

M. Navarro-Tapia[1], G. Burt[2], R. Calaga[1], K. G. Hernández-Chahín[1],
T. Junginger[3], A. Macpherson[1], and R. Torres-Sánchez[1]

[1] Radio Frequency Group, Beams Department, CERN, Geneva, Switzerland.

[2] The Cockcroft Institute, Lancaster University, Daresbury, United Kingdom.

[3] Formerly at CERN; currently at TRIUMF, Vancouver, Canada.

Summary

The performance of the four-rod cavity prototype considered for the HL-LHC upgrade has already been assessed at CERN at cryogenic temperatures three times in the last two years [1, 2, 3]. In this report, the results of the latest measurements, carried out in July 2014, are shown. These measurements were to check the improvement of the cavity performance due to the change of the input and pick-up antennas. An estimation of the residual resistance of the Niobium was also performed.

1 Introduction

The Four-Rod resonator cavity (4Rcav) [4] is one of the candidates considered for the crab-crossing scheme of the LHC luminosity upgrade [5, 6]. A superconducting prototype, made out of Niobium (Nb), was manufactured by Niowave Inc. [7] and then sent to CERN for cold testing.

Among other radio-frequency (RF) performance requirements (see [8] for further details), the cavity resonant frequency must be $f_o = 400.79$ MHz, and the unloaded quality factor has to be $Q_o > 10^{10}$ for a transverse deflecting voltage $V_t = 3.3$ MV at 2 K. According to this, the cavity is expected to have a Nb residual resistance, R_{res}, of the order of 10 nΩ.

Three different tests in cryogenic conditions [1, 2, 3] were already carried out at CERN, during the last two years, for a validation of the RF cavity performance at different states of the cavity processing. The last result showed that $Q_o > 10^9$ at low field levels around 2 K, and the cavity was able to reach up to $V_t = 3.3$ MV before quenching. The Q_o limitation was suspected to be due to the losses in the stainless-steel antennas (both input and pick-up ones) [3].

A fourth measurement was scheduled with new copper antennas to check the improvement in the cavity performance and have an accurate estimation of R_{res}. This note summarizes the new results of the cold testing of the four-rod crab cavity with the new antennas.

2 Difference with the Previous Measurements

In addition to this material change, the input antenna was made shorter than before. In the previous measurements, the cavity was found to be strongly overcoupled, with an input coupling factor $\beta_e \sim 6$ at 4.5 K and $\beta_e \sim 9$ around 2 K ($Q_e \approx 1.2\,10^8$). According to [9], the antenna was shortened by 6 mm to have β_e reduced by a factor of 3.

It is worth mentioning that the 4Rcav had substancial vacuum leaks during all the tests. In a first occasion, knife-edge damages were found in the Niobium-Titanium flanges of the side ports [1]. Despite the repair, the vacuum leak persisted in the following measurements. A visual inspection made while the preparation for the new measurements, concluded with some damages in the beam-pipe flange knife edge and the copper gaskets, as depicted in Fig. 1. Nominally, the beam-pipe flanges were stainless steel. However, a spectroscopy test revealed that the material of the beam-pipe port cannot be classified as stainless steel and, therefore, the material analysis was inconclusive. So, for these measurements, the damaged knife edges were resurfaced with a grindstone and the normal copper gaskets were replaced with annealed ones.

Prior to the cold tests, the 4Rcav has undergone a light chemical etch to remove a few μm, and a subsequent high-pressure water rinse to remove any foreign material remaining on the surface.

In the RF control room, a full revision of all the equipment and connections was done prior to the measurements. A few devices were found to be working out of the 400 MHz band. Some of them, like the directional couplers, did not pose a problem, since they were taken into account in the systematic cable calibration before the measurements. They were replaced by other ones working in the desired frequency range. It was also found that the circulator was tuned at 352 MHz, an inheritance from the LEP (Large Electron-Positron collider) era. The previous measurements showed a standing-wave problem that may be misleading the power measurements. Therefore, it was replaced by a 400 MHz circulator.
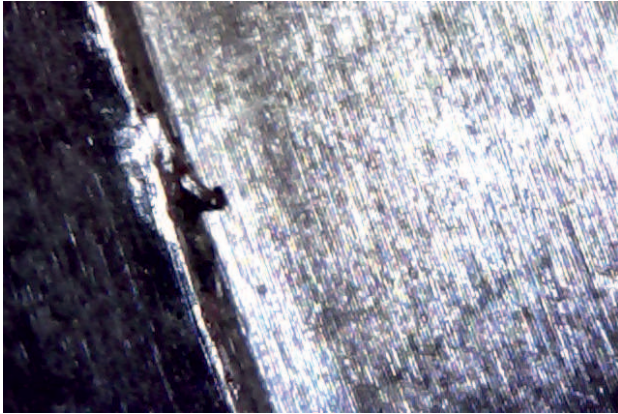
(a) Beam-pipe knife edge. (b) Copper gasket.

Figure 1: Sign of damage in the beam-pipe ports before the measurements.

3 Sensor Setup and Calibration Settings

3.1 Temperature and Second Sound Sensors

A set of cryogenic temperature sensors have been distributed on the outer surface of the cavity. Not only are they used to monitor and safely control the cool-down and warm-up processes, but they are also used to locate hot spots during operation and carry out general thermal diagnostics. Three different kind of sensors were used, each one covering a specific need and a certain temperature range. A brief description of each group is given next.

Cernox™ Resistance Thermometers, from Lake Shore Cryotronics, Inc. Covering the range from 0.1 to 325 K, they are mainly used to follow up the temperature of the Helium bath in the cryostat. Five of them have been distributed from the top to the bottom, even inside one of the rods, as shown in Fig. 2(a).

Allen-Bradley®. These sensors cover the temperatures going from 1.8 K to 5.0 K. They offer a high sensitivity, what make them ideal to monitor in real time the temperature evolution on the cavity surface. Fig. 2(b) shows the placement of the 13 sensors used for this purpose. Note that they were located to cover areas with high magnetic field levels. Some of them are even at the far tip of the rods, to detect a possible local heating on the area.

Ruthenium Oxide (RuO$_2$). This sensor was included for the first time to help with the calibration of the Allen-Bradley® resistors. Their distribution is depicted in Fig. 2(c).

In addition to the thermal sensors, some oscillating superleak transducers (OST) were placed in the insert for quench detection. They detect the time arrival of second-sound waves in superfluid Helium during the cavity quenches. Triangulation is used to determine the location of the defects. A schematic of the OST layout around the vicinity of the cavity is shown in Fig. 2(d).
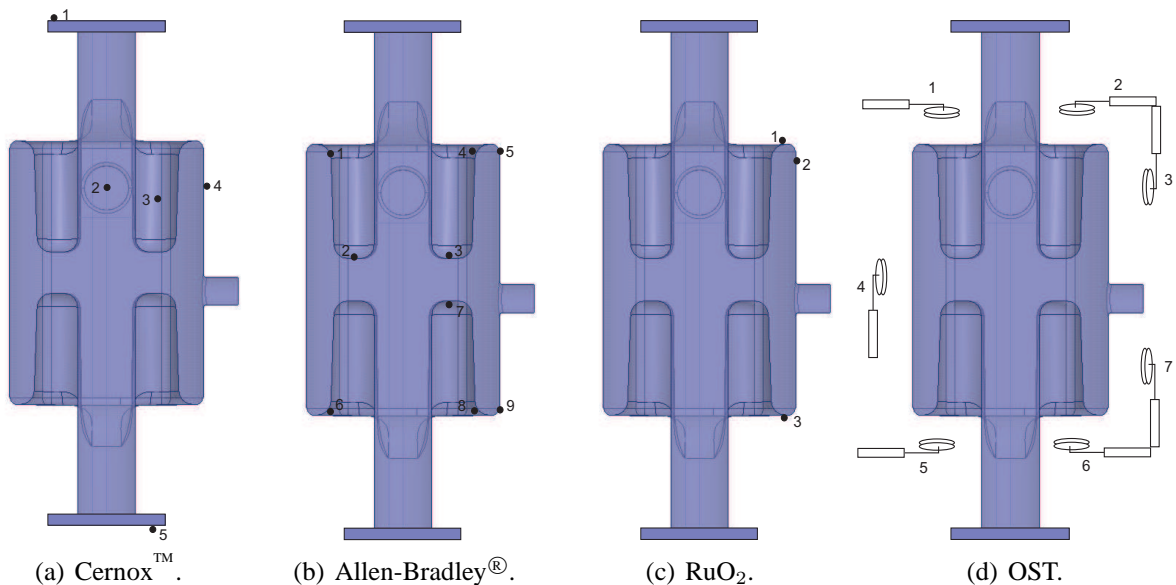

(a) Cernox™. (b) Allen-Bradley®. (c) RuO$_2$. (d) OST.

Figure 2: Sensor placement around the cavity.

3.2 RF Cable Calibration

As shown in Fig. 3, the power meters sampling the forward, reflected and transmitted signals are located far away from the input and output ports of the cavity. The RF cable calibration is a measurement of the attenuation introduced by the cabling and devices lying in between the cavity ports and the power meters, so that a compensation can be applied to the power meter readouts.
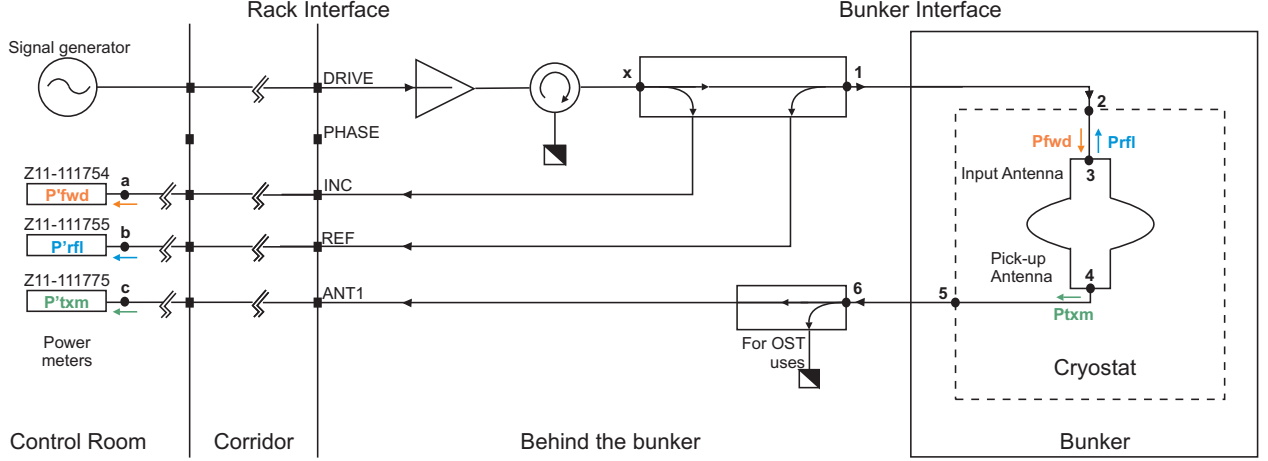

Figure 3: Cable-connection schematic to account for the calibration.

After checking the proper connection of the cables by means of a time-domain reflectometry test, the cable calibration was done following the stepwise procedure given in [10]. Table 1 compiles the attenuation values for the forward, reflected and transmitted paths, done when the cold parts inside the cryostat was at 4.5 K.

It is worth mentioning that the calibration of the cold part was also done at some other temperatures below 4.5 K. The different attenuation values were found to be almost the same, just differing in 0.05 dB at the maximum for 2 K. Therefore, in the following, this small error is neglected and the attenuation values of Table 1 are taken into account for all the temperatures ranging from 2 K to 4.5 K.

Att_{fwd}	Att_{rfl}	Att_{txm}
37.78 dB	41.97 dB	23.19 dB

Table 1: Cable attenuation. Cold part at 4.5 K.

3.3 Cavity Constants

The cavity itself can be characterized by some constants providing the relationship between some important quantities. These constants are needed either to measure Q_o *versus* V_t or computing the surface resistance R_s. They are dependent on the cavity geometry and are typically obtained through a full-wave electromagnetic simulation. A brief definition is given next, together with the numerical results.

- The calibration constant κ relates the stored energy U with the square of the transverse deflecting voltage in the cavity, and is independent of the field level. As shown in Eq. 1, it will be used to obtain V_t from U and calculating the curve Q_o *versus* V_t [11].

$$\kappa = \frac{U}{V_t^2} \qquad [\text{J/MV}^2] \tag{1}$$

4

- The geometry factor G is a cavity constant depending only on the cavity shape, and it is defined by

$$G = \frac{\omega_o \mu_o \int_V |H|^2 \, \mathrm{d}v}{\int_S |H|^2 \, \mathrm{d}s} \qquad [\Omega] \tag{2}$$

where ω_o is the resonant frequency, μ_o is the vacuum permeability and H is the cavity magnetic field. It is related to the surface resistance, R_s, and the unloaded quality factor, Q_o, in the following way:

$$Q_o = \frac{G}{R_s}, \tag{3}$$

which allows a comparison of the performance of different cavities, excluding the wall losses for each specific material. This constant will be eventually used to estimate R_s from the measured Q_o.

The numerical values obtained are shown in Table 2. They were calculated at Lancaster University [12] using CST MICROWAVE STUDIO®.

κ [J/MV^2]	G [Ω]
0.43	59.95

Table 2: Cavity calibration constants from simulations [12].

4   Cool-Down Process

The well-known "Q disease" phenomenon is a residual loss mechanism arising when the hydrogen (H) dissolved in bulk Nb cavities precipitates at the surface, increasing the surface resistance R_s [11]. This effect causes a Q_o degradation that depends on the amount of H dissolved, but also on the cool-down rate of the cavity. Among other cures like ultra-high vacuum baking at high temperatures, a fast cooling-down is advised between 150 K and 50 K, with a cooling rate > 2 K/min.

Moreover, it was recently discovered that the cool-down rate through the transition temperature, T_c, had also a systematic effect on the ambient flux trapped in superconducting Nb cavities [13]. Thus, it is also highly recommended to pass the T_c threshold with a fast cool-down rate (> 2 K/min). For these reasons, a fast cooling rate was applied not only from $150 - 50$ K, but also from 50 K down to 4.4 K through $T_c = 9.25$ K.

It took around 45 minutes to complete the cool-down process. Fig. 4 shows the cool-down evolution for the Cernox™ numbered as 2 (see Fig.2(a)). No thermal cycling was performed.
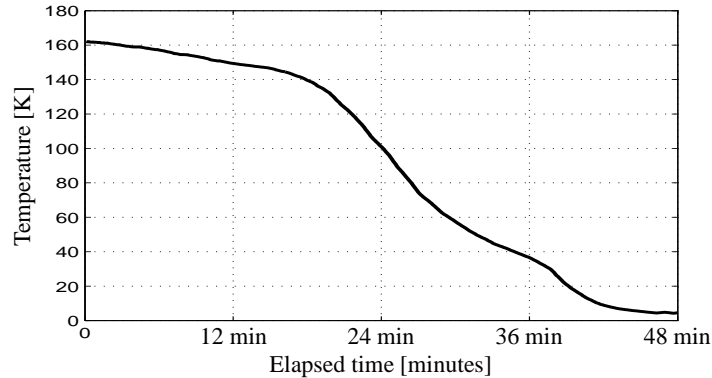

Figure 4: Temperature evolution with time during the cool-down. Cernox™ number 2.

5 Results

5.1 Progress and Plan

The final schedule to carry out the measurements –excluding the cool-down and warm-up processes– was reduced to $3\frac{1}{2}$ days, due to a delay with the cavity preparation and a cryogenic technical stop for maintenance reasons scheduled at the end.

A short description of the measurement progress during these days is next given:

Day 1 Stable condition: $T = 4.45$ K, $P_{\text{cav}} \approx 3\,10^{-7}$ mbar.
   The cavity pressure is still high compared to vacuum levels of the order of 10^{-10} mbar.
   Same stable conditions overnight.

Day 2 Smooth cool-down from 4.45 K to 2.44 K, $P_{\text{cav}} \approx 10^{-7} - 10^{-6}$ mbar.
   Loss of communication with the cryogenic system. Around $2\frac{1}{2}$ hours of stop.
   After the recovery, persistent pressure fluctuations in the cryostat (± 10 mbars/min).
   Cool down to 2.25 K (60 mbar) overnight.

Day 3 Cryogenic software failure overnight. Measurements stopped until midday.
   Smooth cool-down from 2.77 K to 2.40 K, $P_{\text{cav}} \approx 10^{-7} - 10^{-6}$ mbar.
   Half of the cool-down process with pressure fluctuations (± 10 mbars/min).
   Cool down to 2 K (40 mbar) overnight, refilling the cryostat with liquid helium (LHe).

Day 4 Cryogenics failure overnight. The cavity was found at 2.40 K in the morning.
   Cool down to 2 K (40 mbar), without refilling with LHe. $P_{\text{cav}} \approx 2\,10^{-5}$ mbar.
   Cool down to 1.8 K (16 mbar). $P_{\text{cav}} > 2\,10^{-5}$ mbar. Interlock system is OFF.
   Starting warm-up at midday.

As can be readily seen, there were intermittent problems with the cryogenic system, namely communication failures or pressure fluctuations, which forced a complete stop until recovery. The lack of time to stay below the lambda point led to the decision of pumping the cryostat without refilling with LHe, in order to accelerate the process. In this case, the level gauge was continuously supervised, because only the 25% of its length was above the cavity.

All in all, the tight schedule together with these problems left little time for the measurements. Under such circumstances and despite the bad cavity vacuum conditions, it was decided to focus on the acquisition of calibration points at different temperatures while cooling down with stable conditions. Thus, the measurement to be presented are mainly a collection of calibration points and all the analysis around them to estimate the R_{res}. The typical curve Q_o *versus* V_t could only be obtained in a reliable way at 4.5 K.

5.2 The Decrement Method

In order to get the calibration point, the so-called *decrement method*, customarily used to determine high-Q_o values ($> 10^4$), is followed [11, 14]. According to Eq. 4, two main parameters are needed to get Q_o, apart from the resonant frequency, f_o. They are, namely, the time constant τ of the exponential decay of the transmitted signal, and the coupling factors for both the input coupler, β_e, and the trasmitted power coupler, β_t.

$$Q_o = 2\pi f_o \tau (1 + \beta_e + \beta_t). \tag{4}$$

To measure τ, the cavity is excited by a pulsed signal and, during the off period, the transient decay of the natural RF oscillations in the cavity is observed. Fig. 5(a) shows the normalized power
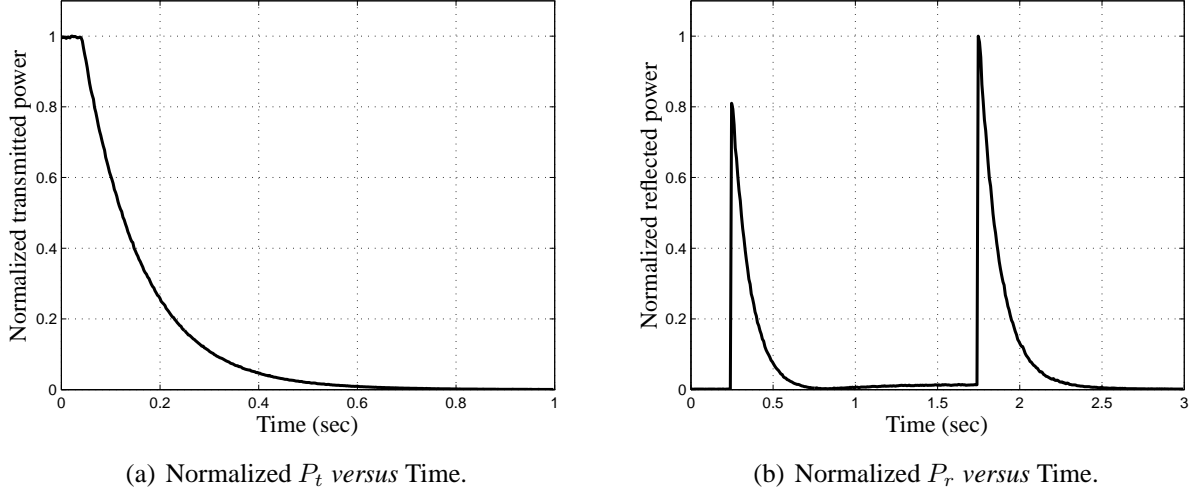
6

(a) Normalized P_t *versus* Time.

(b) Normalized P_r *versus* Time.

Figure 5: Normalized transmitted and reflected power *versus* time at 4.46 K.

trace of the transmitted signal at 4.46 K. The time constant τ is defined as the time needed to have an amplitude decay of $1/e$. Just taking two arbitrary points on the trace, τ can be computed as described in Eq. 5:

$$\tau = \frac{t_2 - t_1}{\ln\left(P_1/P_2\right)} \quad [\text{s}], \tag{5}$$

where P_1 and P_2 are the instantaneous values for the transmitted power at the t_1 and t_2 time instants.

Knowing the coupling factor for both the input coupler, β_e, and the transmitted power coupler, β_t, is essential to get the respective calibration point. In practice, the determination of β_e is done when the cavity is in steady state, from the standard technique measuring the forward and reflected power through the equation:

$$\beta_e = \frac{1 \pm \sqrt{P_r/P_f}}{1 \mp \sqrt{P_r/P_f}}, \tag{6}$$

where the upper sign is used for the overcoupled case, and the lower sign for the undercoupled one. Note that a prior knowledge of the cavity being over- or undercoupled is required beforehand. The qualitative determination of β_e is customarily done by driving the cavity with a train of rectangular pulses. A quick look into the reflected-power waveform gives the hint of the coupling strength.

Fig. 5(b) shows the normalized power trace when at 4.46 K. The second peak being higher than the first one is an indication of the overcoupled state. In this case, the cavity is slightly overcoupled $\beta_e \approx 1.2$ at 4.46 K, what confirms the reduction in the coupling factor as desired. Recall that the input antenna was shortened to decrease β_e by a factor of ~ 3 and, from previous measurements, $\beta_e \approx 6$ at this temperature. Note that the coupling factor will be increasing as the temperature is going down.

For the coupling factor of the pick-up antenna, an easy relationship between the power measurements in continuous wave is enough: $\beta_t = P_t/P_c$, where P_t and P_c are the transmitted signal and the power dissipated in the cavity, respectively.

Once Q_o is known through Eq. 4, having the transverse deflecting voltage V_t is straightforward. V_t is computed by means of the stored energy U and the κ constant as defined in Eq. 1:

$$V_t = \sqrt{\frac{U}{\kappa}} = \sqrt{\frac{Q_o\, P_c}{2\pi f_o \kappa}} \quad [\textbf{MV}]. \tag{7}$$

The couplet (V_t, Q_o) obtained so far through Eq. 7 and Eq. 4, respectively, is also known as the *calibration point*. A calibration constant, referred to as k, is obtained based on this calibration point.

The rest of the curve Q_o *versus* V_t can be measured through power measurements in steady state, with the help of k. The computation of k relies on the fact that the external quality factor of the pick-up antenna, Q_t, is constant for a given temperature and depends only on the geometry. Therefore, the ratio

$$k = \frac{Q_t}{2\pi f_o} = \frac{U}{P_t} \quad [\text{s}]. \tag{8}$$

is constant too. Note that this constant will eventually be responsible of the precise computation of U ($U = kP_t$), which, in turn, will be used to obtain both V_t through Eq. 7, and Q_o through the classical definition:

$$Q_o = \frac{2\pi f_o U}{P_c}. \tag{9}$$

Hence the importance of an accurate estimation of k, since it will considerably affect the whole curve Q_o *versus* V_t.

5.3 List of Calibration Points

As already explained in Sec. 5.1, because of the lack of time and other problems encountered, it was agreed to just measure a collection of calibration points while cooling down smoothly. To get the calibration point, Q_o is measured for a very low transverse voltage V_t, in order to ensure that only the ohmic losses will be present (no field emission or other forms of dissipation).

Table 3 collects the few points that could be measured. It is worth mentioning that although some other measurements were done, they had to be discarded afterwards because of the undesired pressure fluctuations in the cryostat. The different calibration points are sorted by descending temperatures, which are the average value of the Cernox™ sensors. Apart from Q_o and V_t, some other relevant parameters are shown, such as the resonant frequency f_o and the time constant τ, together with the calibration factor k and the different coupling factors.

Note that all the measurements are done for a low transverse deflecting voltage, in this case always around 0.1 MV. The evolution with temperature of f_o and τ is displayed in Fig. 6. As the temperature is going down, both f_o and τ are monotonically increasing, as expected.

The unloaded Q values are shown in Fig. 7. Q_o is increasing for decreasing temperatures, reaching $4\,10^9$ around 2 K. Recall that, in the latest measurements [3], Q_o was just slightly above 10^9 for the same temperature range. This Q_o limitation was believed to be due to the losses of the former stainless-steel antennas. Indeed, changing the antenna material to copper has meant an increase of Q_o by a factor ~ 4 (at 2 K and for low field level).

The evolution with temperature of the coupling factors can also be observed in Table 3. The input antenna coupling factor, β_e, is near to the critical coupling at 4.46 K (see also Fig. 5(b)). Note that the cavity state is always overcoupled but, this time, because the input antenna was shortened,

T [K]	f_o [MHz]	τ [ms]	V_t [MV]	Q_o	k [s]	β_e	β_t	Q_e	Q_t
4.46	400.265	117.22	0.068	$0.754\,10^9$	0.932	1.24	0.32	$6.10\,10^8$	$2.35\,10^9$
3.27	400.279	147.88	0.108	$2.113\,10^9$	0.814	3.65	1.03	$5.79\,10^8$	$2.05\,10^9$
2.90	400.281	155.09	0.104	$2.567\,10^9$	0.677	4.07	1.51	$6.30\,10^8$	$1.70\,10^9$
2.69	400.282	158.70	0.089	$2.568\,10^9$	0.514	3.45	1.99	$7.45\,10^8$	$1.29\,10^9$
2.16	400.283	167.71	0.088	$4.093\,10^9$	0.370	4.31	4.39	$9.50\,10^8$	$0.93\,10^9$

Table 3: Calibration points.
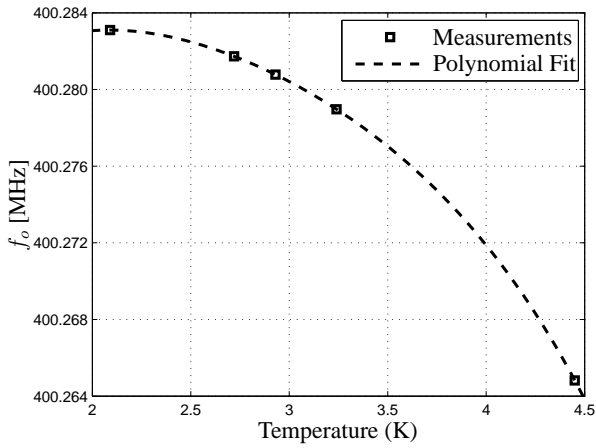
(a) f_o *versus* T.
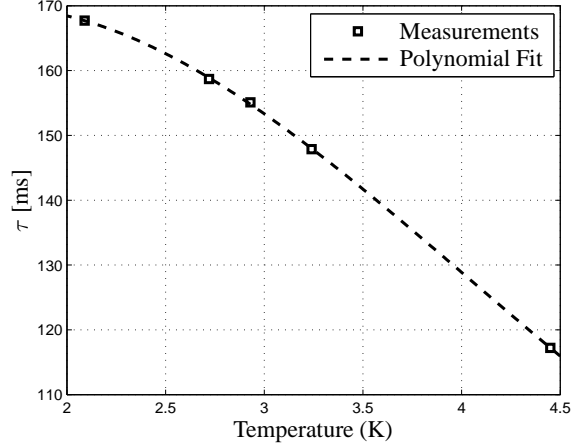
(b) τ *versus* T.

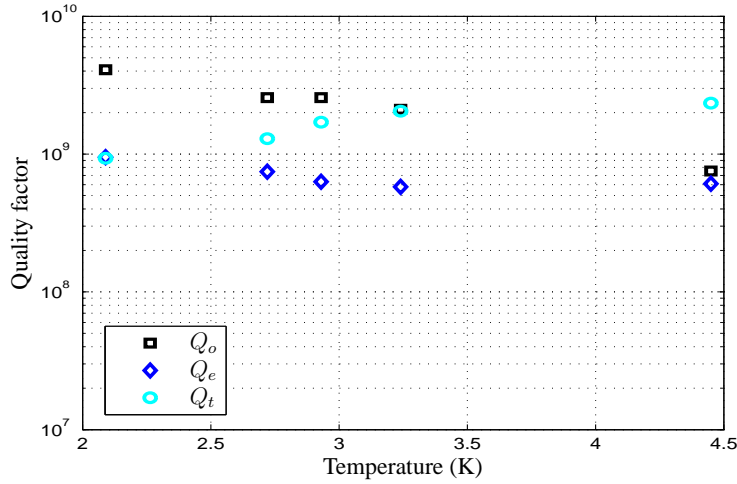Figure 6: Resonant frequency and decay constant *versus* temperature for low field level.

Figure 7: Q *versus* T.

$\beta_e < 5$ for all the temperature range. These results confirms a reduction of β_e by approximately a factor 3 with respect to the previous measurements [3].

Looking at the coupling factor for the pick-up antenna, β_t, it only remains undercoupled at 4.46 K. Ideally, the pick-up antenna should be weakly coupled, i.e., $\beta_t \ll 1$, at the low temperature range. However, it seems that Q_t is in the 10^9 range, instead of the $6 \, 10^{10}$ that was numerically calculated [15], meaning that the pick-up antenna has to be shortened.

The external Q for both the input and pick-up antennas, Q_e and Q_t, can be derived using the data of Table 3 ($Q_e = Q_o/\beta_e$, $Q_t = Q_o/\beta_t$). They have also been compiled in the table and plotted in Fig. 7 against the temperature. It shows how $Q_e \sim 10^8$ and $Q_t \sim 10^9$, which is not as high as expected.

The calibration factor k is also shown in Table 3, showing a strong dependency on the temperature. Although this dependency is still not well understood, some possible reason could be the thermal contraction of the pick-up antenna.

5.4 Residual Resistance Analysis

The microwave surface resistance R_s of superconductors is proven to be dependent on the temperature [11]. However, below a certain temperature, in the limit $T \to 0$, the experimental data reveals that R_s saturates at a non-zero value, called residual resistance R_{res}. A very good approximation of R_s is given by the following equation:

$$R_s(T) = R_{\text{res}} + \frac{A\,\omega^2}{T} \exp\left(-\frac{\Delta}{k_B T}\right), \tag{10}$$

where A is a factor depending on the material parameters, Δ is the superconducting gap, and k_B is the Boltzmann constant ($k_B = 8.617\,10^{-5}$ eV/K). Note that Δ also depends on T, meaning that this approximation is only valid for $T < T_c/2$, when $\Delta(T)$ has reached its asymptotic value [11]. By definition, then,

$$R_{\text{res}} = \lim_{T \to 0} R_s(T). \tag{11}$$

By means of Eq. 3, the surface resistance can be computed for all the calibration points listed in Table 3, using the geometric factor $G = 59.95\ \Omega$ as given in Table 2. The results are collected in Table 4, and displayed in Fig. 8. As expected, R_s decreases exponentially with temperature and saturates at R_{res}. A numerical fitting has been done and is also represented, yielding a $R_{\text{res}} \approx 15.7\ \Omega$, for a gap $\Delta = 1.87$ meV. This is a very promising result, within the range of the 10 to 20 $n\Omega$ of a well-prepared Nb surface. Recall that the first measurements yielded a residual resistance of about $90 - 100$ nΩ [1]. Notice that the R_{res} value coming from the fitting is somewhat higher than the R_s value at 2 K. This fact is just due to the uncertainty when trying to fit an exponential with very few points.

T [K]	4.46	3.27	2.90	2.69	2.09
R_s [nΩ]	79.48	28.37	23.36	23.34	14.65

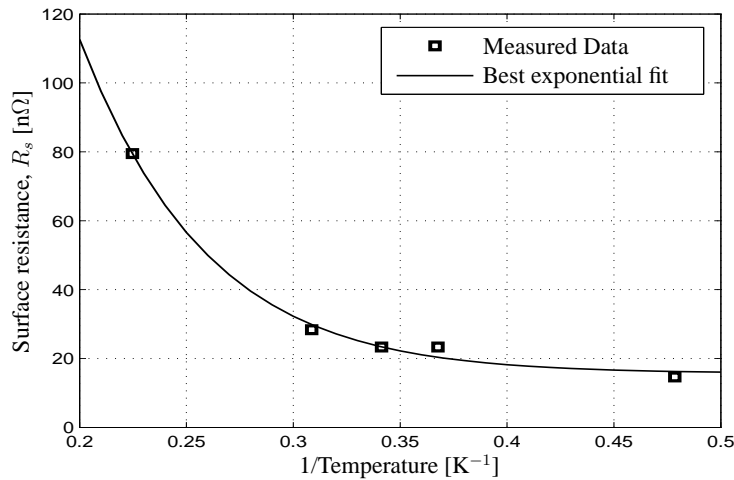Table 4: Surface resistance as a function of temperature.

Figure 8: Surface resistance *versus* temperature. Measurements and numerical fitting. $R_{\text{res}} \approx 15.7\ n\Omega$ (see Eq. 11), $\Delta = 1.87$ meV.

5.5   Unloaded Q *versus* V_t

As already mentioned in Sec. 5.1, the curve Q_o *versus* V_t could only be obtained at 4.5 K. This measurement was done in pulsed-mode conditions, i.e., when no local sign of heat is present in the cavity. To that end, the Allen Bradley readouts were continuously checked, and the next measurement point was not taken until the initial cavity temperature was recovered and homogeneous.

Fig. 9 shows the Q_o measurements as a function of the deflecting voltage, together with the constant lines of dissipated power in the cavity, P_c (in watts). The corresponding calibration point, provided in Table 3, is also shown as a red cross. Compared to the latest measurement made in December 2013 [3], the performance is very similar at around 4.5 K. The starting Q_o value is slightly better now for low V_t, but the slope is steeper at high V_t before quenching. Some multipactor-like activity was found at around $V_t \approx 0.3$ MV.

As a kind of cross-check of the goodness of the Q_o-*versus*-V_t trace, both the input and pick-up antenna quality factors, Q_e and Q_t, have been derived and plotted in Fig. 10. These quantities only depend on the cavity and the coupler geometries, and not on the accelerating field or deflecting voltage. Thus, they should stay constant and stable with V_t, unless any other ways of dissipation, different from the ohmic losses, are present. It can be seen how Q_t remains constant on the entire range. However, Q_e start decreasing at around $V_t = 1.5$ MV, at the same time that the onset of the level of radiation (see right-hand vertical axis).
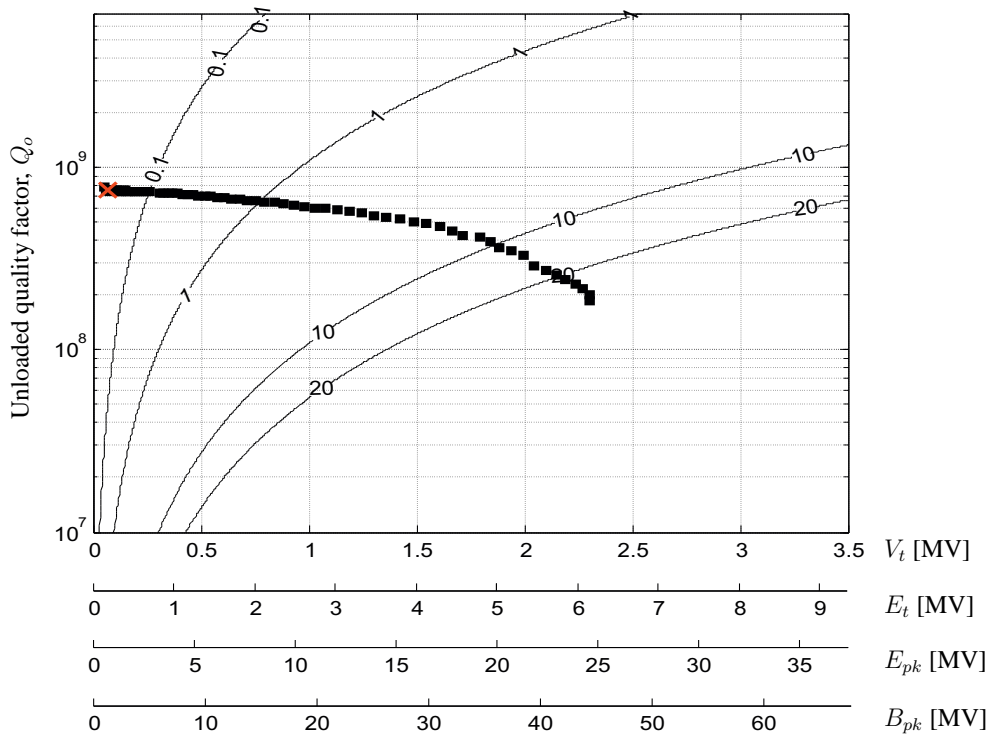

Figure 9: Unloaded quality factor *versus* transverse deflecting voltage at 4.46 K. In red: the calibration point. Lines of constant dissipated power in the cavity also shown (in watts).
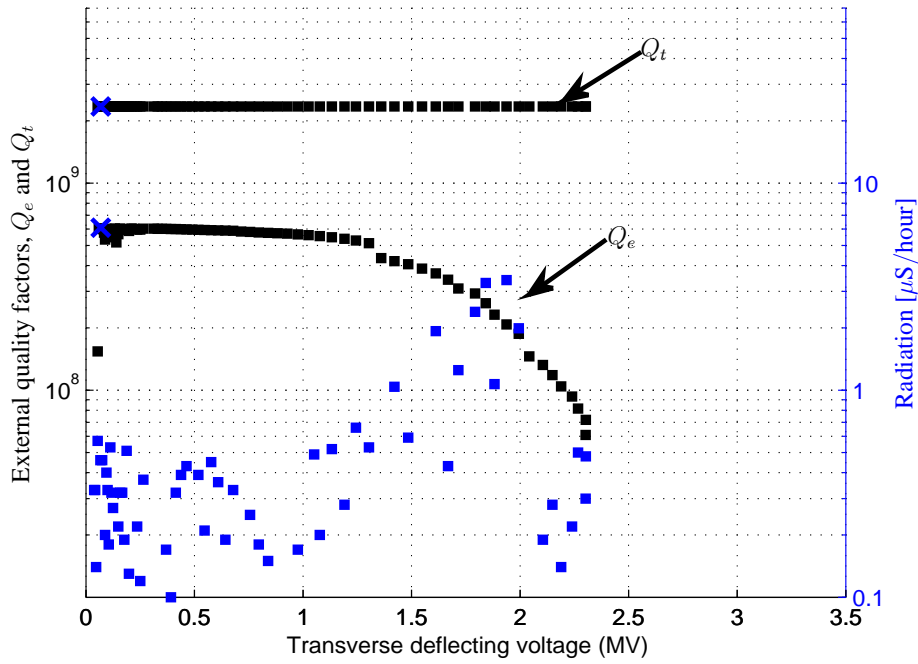
Figure 10: External quality factors and radiation level *versus* transverse deflecting voltage at 4.46 K.

5.6 Lower Order Mode

The 4Rcav has a lower-order mode 25 MHz apart from the fundamental one, i.e., at around 374.25 MHz. A look to the transmitted signal at this frequency was taken at 3.9 K, as shown in Fig. 11 in the frequency domain. The 3 dB bandwidth is approximately around 1 kHz. This bandwidth is consistent with a time decay τ of around 0.16 milliseconds, too fast to be measurable with the spectrum analyzer. So no calibration point could be taken for the lower-order mode at this temperature.
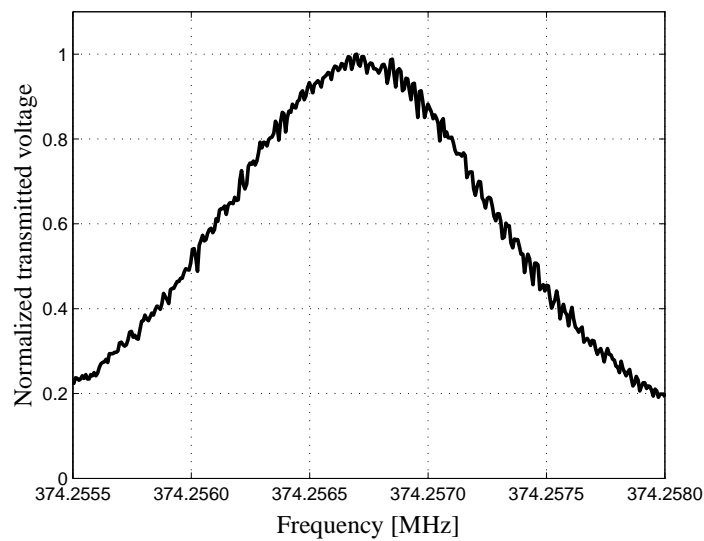

Figure 11: Normalized transmitted signal for the lower-order mode.

6 Warm-Up Process

The warm-up process from 4.5 to 80 K was fully monitored and the main observable parameters were recorded for subsequent analysis.

6.1 Temperature Evolution with Time

The overall tendency of the warming up can be seen in Fig. 12(a), which shows the temperature evolution of the Cernox™ with time. The average and $\pm 2\sigma$ standard-deviation error bars are shown for the 3 sensors with less dispersion between them (Cernox™ numbered as 2, 3 and 4 in Fig. 2(a)). Looking at the error bars, it is readily seen that the Cernox™ used are more consistent and accurate in the temperature range $0 - 10$ K. It took almost 6 hours to go from 4.5 K to above the critical temperature, T_c. From the slope of the curve, it is worth noting that warm-up gradient rate of the superconducting state differs from that of the normal state.

Fig. 12(b) shows a detailed view of the temperature evolution around the transition zone. An unexpected *blip* (decreasing temperature) is happening around the critical temperature. This phenomenon is still not understood by the authors. A possible reason could be that the cryostat pressure presented some fluctuations while warming up.

From now on, whenever a parameter is represented *versus* temperature, the averaged curve of Fig. 12(a) will be used, with a correction applied to smooth the behavior around the critical temperature.

6.2 Resonant Frequency and Other Parameters *versus* Temperature

A Vector Network Analyzer (VNA) (*Agilent Technologies* E5071C) was connected to the cavity from the RF control room to track the change in resonant frequency, f_o, while the warm-up process. This change in f_o is plotted against the temperature evolution and shown in Fig. 13(a). As long as the cavity is getting warmer and warmer, f_o is monotonically decreasing, with a sudden change of a few kHz happening around the transition from superconducting to normal-conducting state.

Likewise, an automatic tracking of the 3 dB bandwidth, $\Delta f_{3\mathbf{dB}}$, of the transmission parameter S_{21} was performed. Fig. 13(b) shows the increasing tendency as the cavity is warming up. Again, a
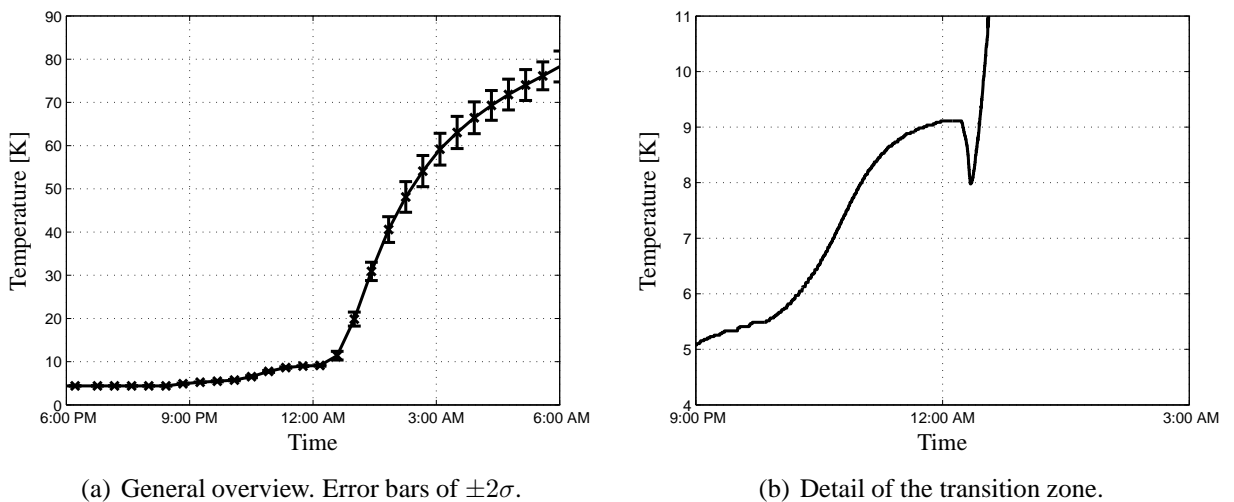

(a) General overview. Error bars of $\pm 2\sigma$.

(b) Detail of the transition zone.

Figure 12: Temperature *versus* time during the warm-up process. Cernox™ number 2, 3 and 4.

sudden change from less than 100 Hz in the superconducting state to tens of kilohertz in the normal state can be appreciated.

Both the drop in f_o and the increase in $\Delta f_{3\mathbf{dB}}$ around the transition zone have, therefore, an impact in the loaded quality factor, Q_L, around T_c. Fig. 13(c) presents the loaded Q computed as $Q_L \approx f_o/\Delta f_{3\mathbf{dB}}$. Q_L decreases quickly from several 10^6 to a few 10^4 while crossing the transition zone. Note the big uncertainty committed when computing Q_L in the superconducting state, mainly due to the difficulty to accurately estimate the $\Delta f_{3\mathbf{dB}}$ in that region.
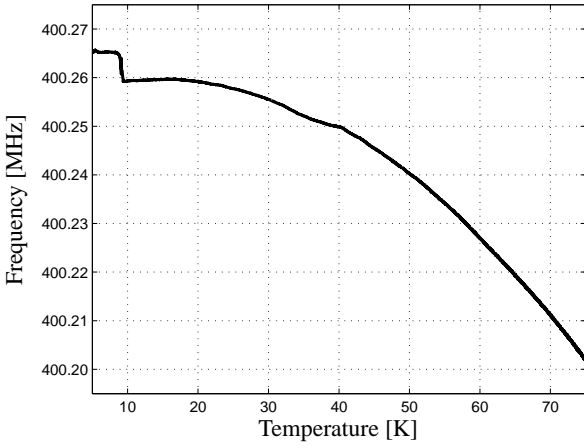
(a) Resonant frequency *versus* Temperature.
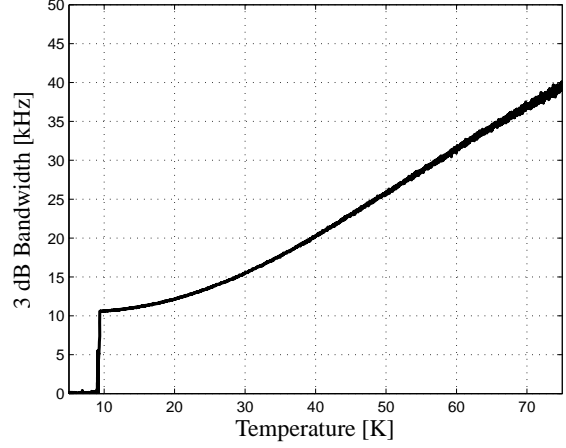
(b) 3 dB bandwidth *versus* Temperature.
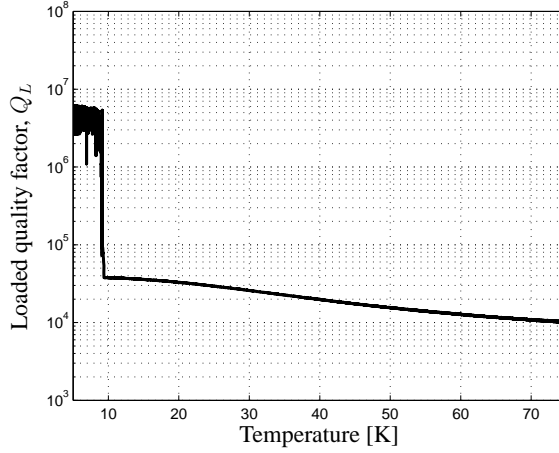
(c) Loaded quality factor *versus* Temperature.

Figure 13: Evolution of some important parameters during the warm-up process.

7   Conclusion

The performance of the 4Rcav has been tested once more at cryogenic temperatures. The main difference with respect to the previous measurements is the change of material of the input and pick-up antennas from stainless steel to copper. Due to some time constraints only a collection of calibration points were mainly measured. The unloaded quality factor was around 4 times higher than before, i.e., $Q_o \approx 4\,10^9$ at around 2 K. This increase in Q_o may be attributed to the new copper antennas, as expected. In addition, an estimation of the residual resistance has been made, yielding a $R_{\text{res}} \approx 15$ nΩ. This value means an improvement compared to the first measurements were R_{res} was about $90 - 100$ nΩ.

Acknowledgements

References

[1] P. Ambattu, L. Alberty, G. Burt, R. Calaga, O. Capatina, S. Calatroni, E. Ciapala, D. Doherty, L. Ferreira, E. Jensen, B. Hall, C. Lingwood, P. Maesen, A. Mongelluzzo, T. Renaglia, and M. Therasse, First Test Results of the 4-Rod Crab Cavity, *Proceedings of IPAC'13*, Shanghai, China.

[2] R. Calaga, and E. Jensen, LHC Crab Cavity Progress and Outlook, *Proceedings of SRF'13*, Paris, France.

[3] B. Hall, G. Burt, T. Jones, S. Pattalwar, N. Templeton, A. J. May, A. E. Wheelhouse, P. A. McIntosh, R. Calaga, S. Calatroni, E. Jensen, and A. MacPherson, Testing and Dressed Cavity Design for the HL-LHC 4R Crab Cavity, *Proceedings of IPAC'14*, Dresden, Germany.

[4] B. Hall *et al.*, LHC-4R Crab Cavity, Prosented at *2nd Joint HiLumi LHC-LARP Annual Meeting*, Frascati, Italy, 14-16 Nov. 2012.

[5] High Luminosity Large Hadron Collider HL-LHC, `http://hilumilhc.web.cern.ch`

[6] R. Calaga *et al.*, Crab Cavities for the LHC Upgrade, *Proceedings of Chamonix*, Chamonix, 2012.

[7] G. Burt, Manufacture of a Compact Prototype 4R Crab Cavity for HL-LHC, *Proceedings of IPAC'13*, Shanghai, China, May 2013.

[8] P. Baudrenghien, K. Brodzinski, R. Calaga, O. Capatina, E. Jensen, A. Macpherson, E. Montesinos, and V. Parma, *Functional Specifications of the LHC Prototype Crab Cavity System*, CERN-ACC-NOTE-2013-003, February 2013.

[9] M. Navarro-Tapia and R. Calaga, *Quality-Factor Measurements versus the Input Coupler Length for the Four-Rod LHC Crab Cavity at Room Temperature*, CERN note to be published.

[10] M. Navarro-Tapia, R. Torres-Sanchez, K. G. Hernández Chahín, and A. Macpherson, "Cable Calibration Procedure for Vertical Tests of SRF Cavities at SM18-V3", EDMS note. `https://edms.cern.ch/document/1454709/1`.

[11] Hasan Padamsee, Jens Knobloch and Tom Hays, *RF Superconductivity for Accelerators,* New York: John Wiley & Sons, 1998.

[12] G. Burt and B. Hall, Private communication.

[13] A. Romanenko, A. Grassellino, O. Melnychuck, and D. A. Sergatskov, Dependence of the Residual Surface Resistance of Superconducting RF Cavities on the Cooling Dynamics Around T_c, *arXiv:1401.7747 [physics.acc-ph]*.

[14] Edward L. Ginzton, *Microwave Measurements,* New York: McGraw-Hill, 1957.

[15] R. Calaga *et al.*, *4R Test Program SM18: Surface Treatment & Testing of 4R Cavity*, Internal Communication (`http://rcalaga.web.cern.ch/rcalaga/LHCCRABS/`).